

Supplementary Information for

Profound Influence of Surface Trap States on the Utilization of Charge Carriers in CdS Photoanodes

Elif Öykü Alagöz^{1,2}, Hadi Jahangiri³, Sarp Kaya^{1,2,*}

¹ Department of Chemistry, Koç University, 34450 Istanbul, Türkiye

² Koç University Tüpraş Energy Center (KUTEM), 34450 Istanbul, Türkiye

³ Koç University Surface Science and Technology Center (KUYTAM), 34450 Istanbul, Türkiye

*Corresponding author: sarpkaya@ku.edu.tr (Sarp Kaya)

Materials and Chemicals

Cd(NO₃)₂·4H₂O (≥98%), NH₂CSNH₂ (≥99.0%), C₁₆H₃₃N(CH₃)₃Br (≥98%), NaOH, Na₂SO₃, and H₂O₂ (34.5-36.5%) were purchased from Sigma-Aldrich. Fluorinated tin oxide (FTO) coated glass substrates were purchased from Ossila. All electrolytes and solutions used in the synthesis and characterization experiments were prepared with deionized (DI) water.

Synthesis of CdS Photoanodes

Fabrication of FTO/CdS Photoanodes: The CdS photoanodes were prepared using a surfactant-free hydrothermal deposition method inspired by the procedures reported elsewhere^{1,2}. 0.8543 g Cd(NO₃)₂·4H₂O (1.2 mmol) and 0.3875 g thiourea (2.4 mmol) were dissolved in 40 ml DI water and stirred for 20 min. until the mixture became homogeneous. The FTO substrate was cleaned by sonication in acetone, ethanol, and DI water for 10 min. each. The cleaned FTO substrate was placed on its conductive side facing down in a Teflon-sealed stainless-steel autoclave. The reaction solution was transferred to the autoclave and kept at 200 °C for 8 h. Subsequently, the resulting sample was washed with DI water multiple times and annealed at 400 °C for 1 h at a heating rate of 5 °C.min⁻¹ under continuous nitrogen flow in a tubular furnace.

Fabrication of FTO/CdS/CTAB Photoanodes: As prepared CdS photoanodes were coated with CTAB by using a facile dip-coating method³. 0.03 M CTAB solution was prepared by dissolving 0.34 g CTAB in 30 ml DI water. The mixture was stirred until it is completely homogeneous. The hydrothermally deposited CdS photoanodes were placed vertically in the CTAB solution during continuous stirring to prevent the precipitation of CTAB. The amount of CTAB overlayer was controlled by increasing the dip coating time. After the dip-coating, the photoanodes were dried at 60 °C for 8 h.

Fabrication of CTAB-Decorated Powder CdS for TEM: CdS nanorod powder samples were prepared using the same hydrothermal synthesis procedure. After the synthesis, CdS dispersed in DI water was collected from the bottom of the autoclave. The mixture was washed and centrifuged in ethanol and DI water to remove impurities or unreacted precursors. Subsequently, the powder was dried in the oven at 60 °C for 8 h. The resulting product was annealed at 400 °C for 1 h with a heating rate of 5 °C.min⁻¹ under continuous nitrogen flow. 65 mg CdS powder was weighed and kept in 1.5 ml 0.03 M CTAB solution stirring continuously at 90 rpm for 6 h. After CTAB treatment, the CTAB/CdS powder was collected and dried in the oven at 60 °C for 8 h.

Creating S_vs on the CdS Photoanode Surface: To confirm the proposed adsorption behavior of CTAB on the CdS surface, H₂O₂ treatment method⁴ was used to create S_vs. As prepared CdS photoanodes were dipped in 5 M H₂O₂ solution for 60 s and left air drying overnight.

Photoelectrochemical Characterization All PEC experiments were performed using a Biologic VSP300 potentiostat and a 3-electrode configuration where Ag/AgCl is the reference electrode, Pt is the counter electrode, and CdS is the working electrode in a quartz cell purchased from Pine Research. 0.1 M NaOH (pH = 12.87) was used as the electrolyte in all experiments. All potentials in the graphs were converted to the reversible hydrogen electrode (RHE) scale using the Nernst Equation⁵. Electrochemical surface areas (ECSA) of the photoanodes were determined by capacitance measurements. Cyclic voltammetry (CV) scans were recorded in the dark using different potential scan rates between 25 and 400 mV.s⁻¹. Current density differences in cathodic and anodic cycles were plotted against the potential scan rates and the slope of this plot was used to compare the ECSA. An Oriol LCS-100 solar simulator with a 1.0 Sun AM 1.5G filter was used as the light source for LSV, EIS, and open circuit potential (OCP) experiments. Incident photon-to-current efficiency (IPCE) measurements were performed by using a 300 W Xe lamp with a Newport monochromator as the light source.

Structural Characterization: Bruker D2 Phaser X-Ray Diffractometer was used to identify the crystal phase purity of the photoanodes via X-ray diffraction (XRD). The surface electronic structure of the photoanodes was analyzed by using a Thermo K-alpha X-ray photoelectron spectroscopy (XPS) instrument with an Al K α light source. Fourier transform infrared (FTIR) measurements were done by using a Thermo Scientific iS10 FTIR instrument. A Shimadzu UV-3600-UV-Vis-NIR Spectrophotometer was used to measure the reflectance of the

photoanodes. The reflectance values were transformed to absorbance by using Kubelka-Munk calculation ⁶. The absorbance data was used to determine the band-gap energy of the photoanodes. In-situ PL measurements were performed by using an FLS1000 spectrometer from Edinburgh Instruments. A Zeiss Evo LS15 field emission scanning electron microscope (FESEM) and energy dispersive X-ray spectroscopy (EDX) were used to analyze the morphology of the photoanodes and their elemental composition. High-resolution transmission electron microscopy (HRTEM) images and HRTEM-EDX spectroscopy were performed for elemental mappings by using a Hitachi HF5000 200kV high-resolution transmission electron microscope.

Tauc Analysis for Band-gap Energy Determination: UV-Vis spectroscopy was used to investigate the optical properties of the photoanodes. Band-gap energies were calculated by the using Tauc formula shown in Equation S1.

$$(\alpha h\nu)^n = B(h\nu - E_g) \quad \text{Equation S1}$$

Herein, α is the absorption coefficient, h is Planck's constant, ν is the frequency of the incident photon, n is the index for allowed transitions and it is taken as 2 since CdS is a direct band-gap semiconductor ⁷. B is the proportionality constant, and E_g is the band-gap energy. In order to calculate E_g for each sample, reflectance measurement was performed and the Kubelka-Munk function was applied. Details of the Kubelka-Munk and Tauc relation can be found elsewhere ⁸.

Determination of IPCEs: IPCE of the photoanodes were calculated by using the formula below ⁹:

$$\text{IPCE} = \frac{|j_p - j_d| \times 1240}{\lambda \times P_{\text{in}}} \quad \text{Equation S2}$$

where j_p is the photocurrent density under illumination, j_d is the dark current ($\text{mA}\cdot\text{cm}^{-2}$), λ is the incident photon wavelength (nm) and P_{in} is the power intensity of the incident photon at the respective wavelength ($\text{mW}\cdot\text{cm}^{-2}$).

Calculation of the Injection Efficiency (η_{inj}): LSV measurements under continuous illumination were performed in 0.1 M NaOH and 0.1 M NaOH / 0.25 M Na_2SO_3 electrolyte separately. The injection efficiency (η_{inj}) was calculated by the formula given below ¹⁰.

$$\eta_{inj} = \frac{j_{NaOH}}{j_{NaOH/Na_2SO_3}} \quad \text{Equation S3}$$

Where j_{NaOH} and j_{NaOH/Na_2SO_3} are the photocurrent densities at certain potentials in 0.1 M NaOH and 0.1 M NaOH / 0.25 M Na₂SO₃ electrolyte respectively.

Electrochemical Impedance Spectroscopy (EIS) and Nyquist Fittings: EIS measurements were performed between 100 kHz to 100 mHz within the LSV potential range starting from 0.2 V which is close to the onset region. Nyquist plot fittings were performed by using Randle's circuit model ¹¹ and charge transfer resistance (R_{CT}) was obtained.

Mott-Schottky (MS) Analysis: MS analysis was performed to investigate the change in band bending characteristics which are flat-band potential (V_{fb}) and donor density (N_d) by the equation shown below:

$$\frac{1}{C^2} = \frac{2}{\epsilon \epsilon_0 A^2 e N_d} \left(V - V_{fb} - \frac{k_B T}{e} \right) \quad \text{Equation S4}$$

In Equation 4, C is the differential capacitance with respect to potential, ϵ is the dielectric constant, ϵ_0 is the vacuum permittivity, A is the coated area, e is the elementary charge, V is the applied potential, k_B is the Boltzmann constant, and T is the temperature.

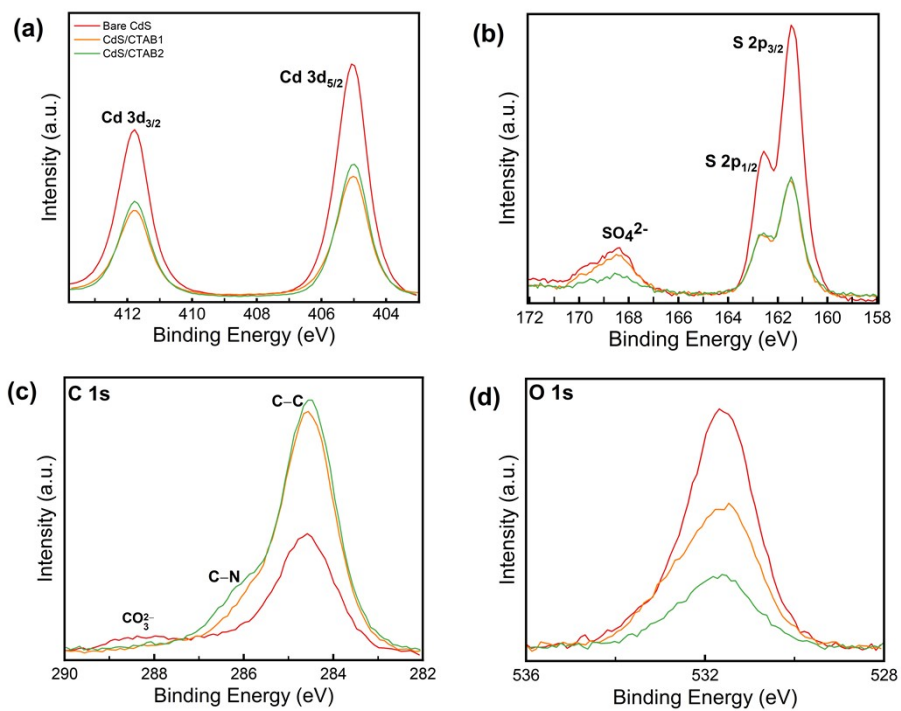


Figure S1. (a) Cd 3d, (b) S 2p, (c) C 1s, and (d) O 1s XPS spectra of bare CdS, CdS/CTAB1, and CdS/CTAB2.

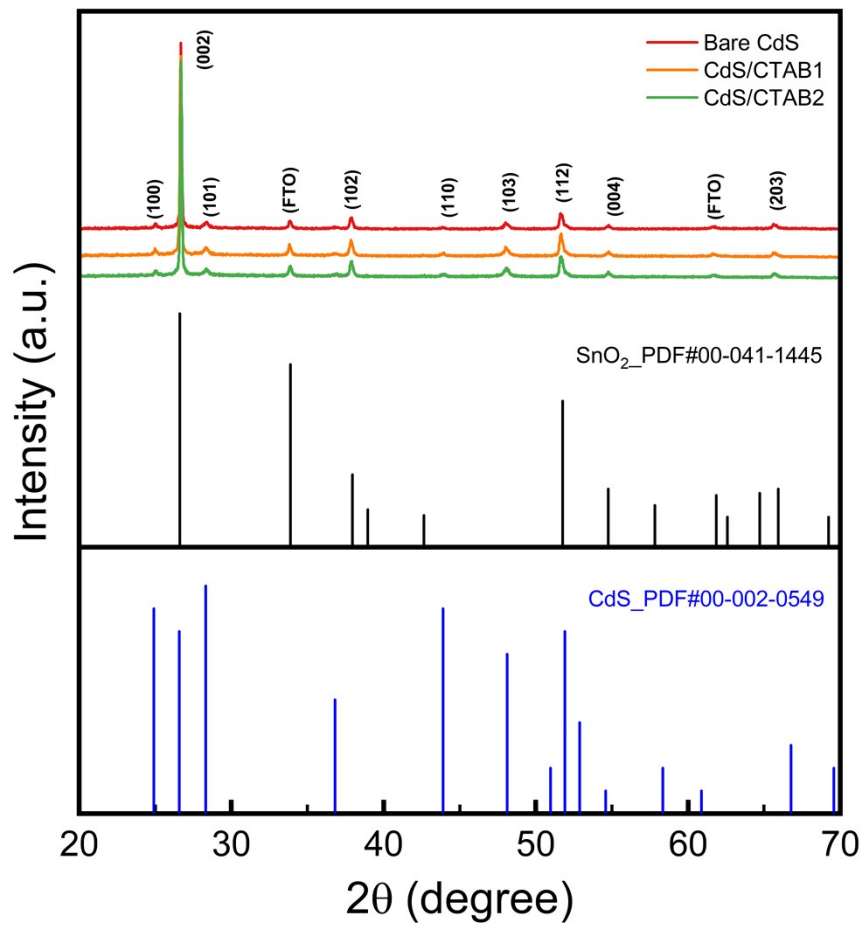


Figure S2. XRD data of bare CdS, CdS/CTAB1, and CdS/CTAB2.

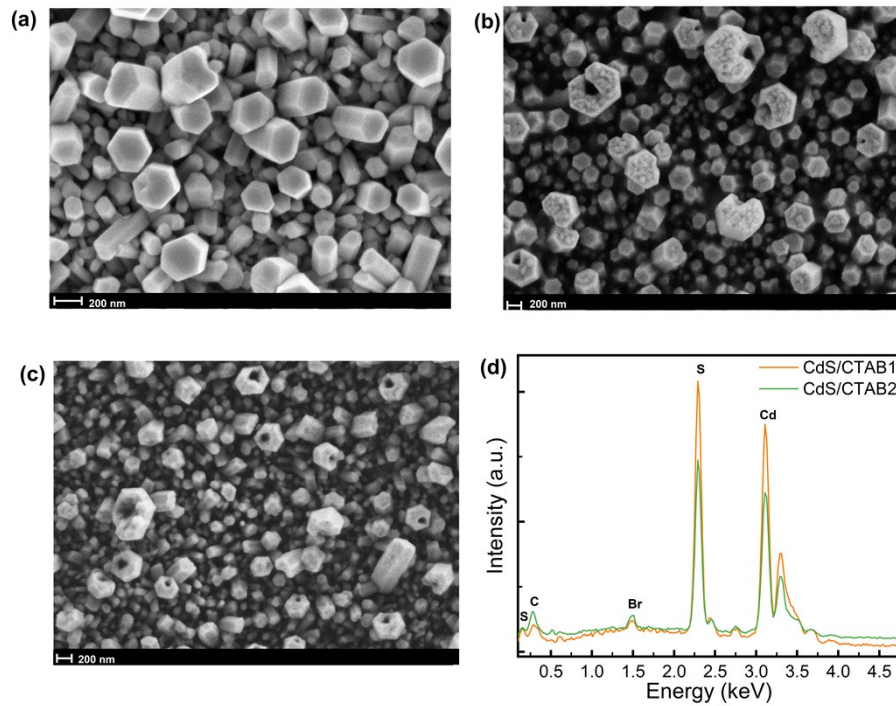


Figure S3. FESEM images of (a) bare CdS, (b) CdS/CTAB1, and (c) CdS/CTAB2. (d) EDS spectra of CdS/CTAB1 and CdS/CTAB2.

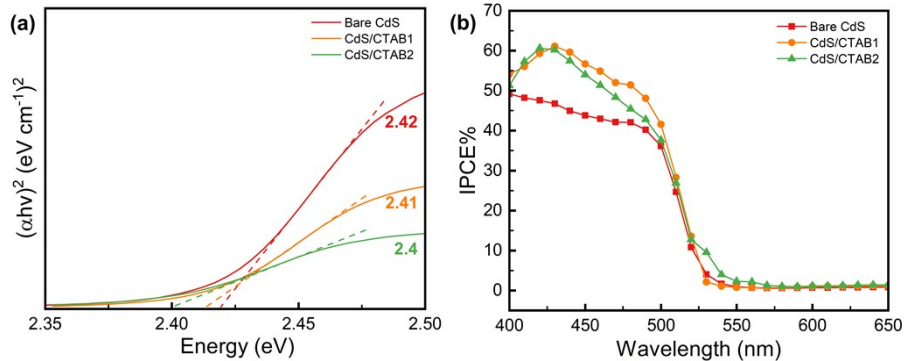


Figure S4. (a) Tauc plots and (b) IPCE efficiencies of bare CdS, CdS/CTAB1, and CdS/CTAB2 measured at 1.2 V_{RHE}.

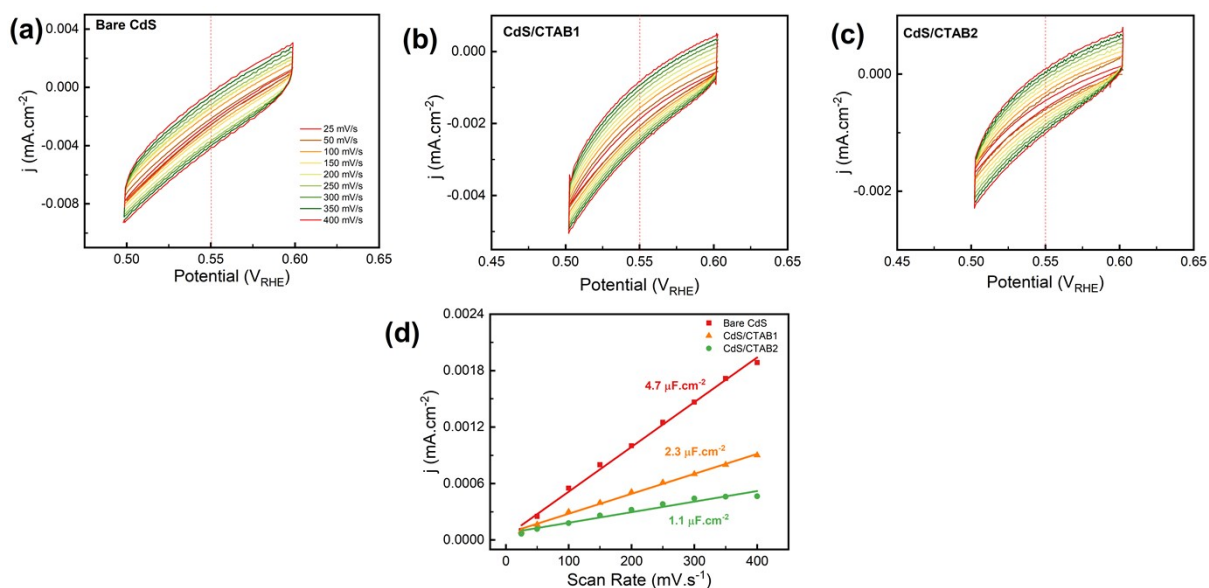


Figure S5. CV measurements at different scan rates of (a) bare CdS, (b) CdS/CTAB1, and (c) CdS/CTAB2. (d) ECSA plots of the photoanodes.

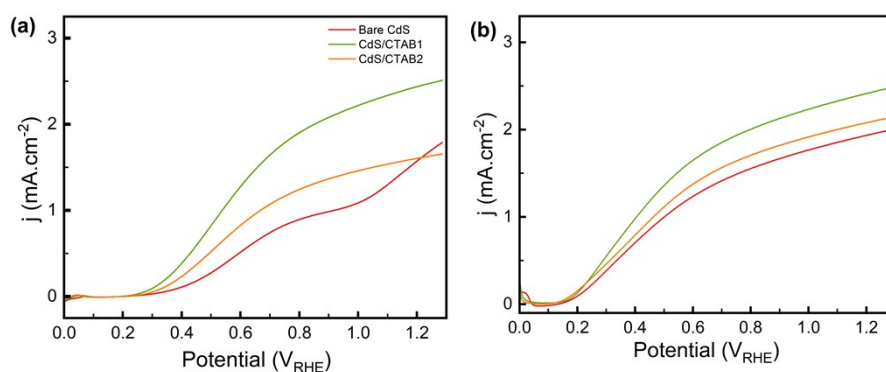


Figure S6. LSV of bare CdS, CdS/CTAB1, and CdS/CTAB2 in (a) 0.1 M NaOH and (b) 0.1 M NaOH / 0.25 M Na $_2$ SO $_3$. Measurements were performed with a 50 mV \cdot s $^{-1}$ potential scan rate under continuous illumination. These voltammograms were used to calculate η_{inj} .

Nyquist plots were fitted using Randle's model given in Figure S7a. In this model, R_S is the resistance of the electrolyte, R_{CT} is the charge transfer resistance at the photoanode/electrolyte interface, and CPE is the constant phase element to represent the imperfect capacitive behavior of CdS¹². R_{CT} values in Figure 3b were determined from the second x-intercept of the Nyquist plots shown in Figure S7b, S7c, and S7d.

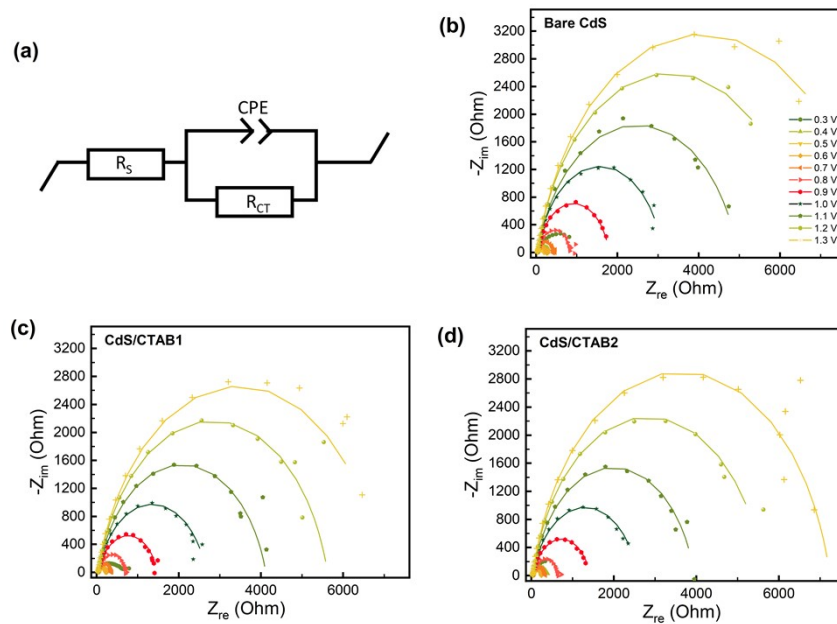


Figure S7. (a) Randle's model circuit used for Nyquist plot fittings of bare CdS, CdS/CTAB1, and CdS/CTAB2. EIS fittings of (b) bare CdS, (c) CdS/CTAB1, and (d) CdS/CTAB2.

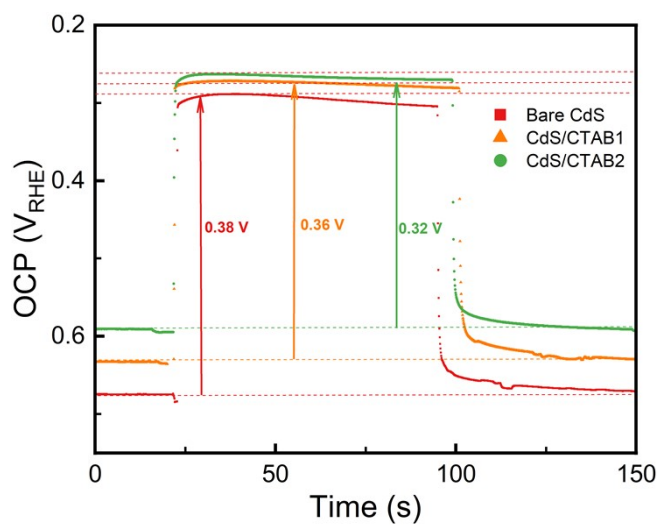


Figure S8. Transient OCP measurements with chopped illumination.

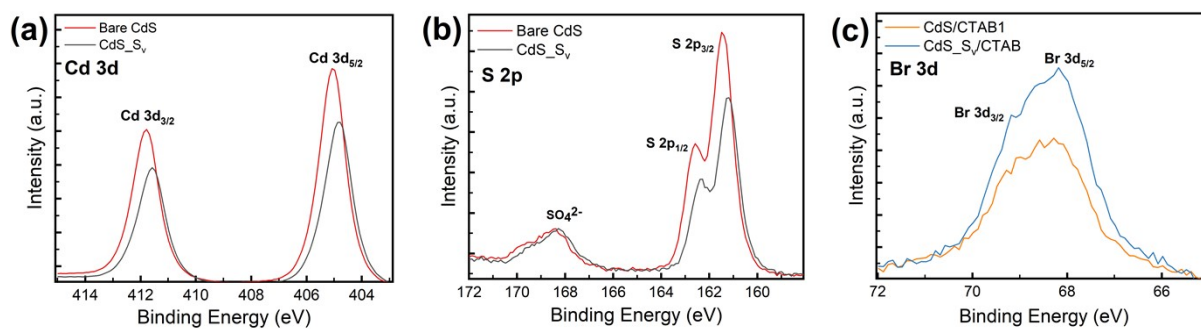


Figure S9. (a) Cd 3d and (b) S 2p spectra of bare CdS and CdS_{S_v}, and (c) Br 3d spectra of CdS/CTAB1 and CdS_{S_v}/CTAB.

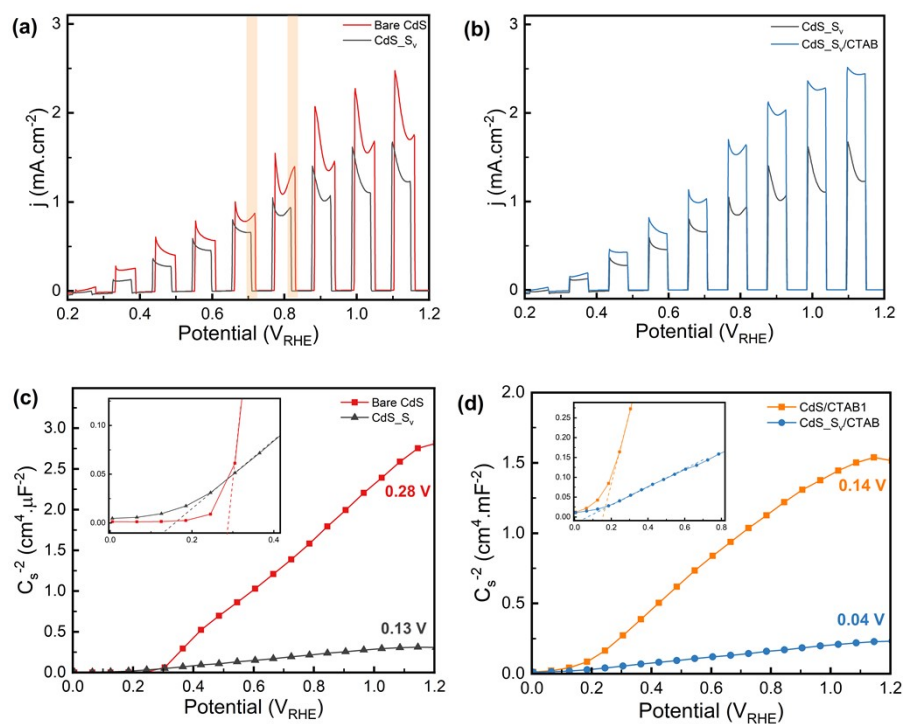


Figure S10. Chopped light LSV of (a) bare CdS after and CdS_{S_v}, (b) CdS_{S_v} and CdS_{S_v}/CTAB. MS plots of (c) bare CdS and CdS_{S_v}, (d) CdS/CTAB1 and CdS_{S_v}/CTAB.

Table S1. Atomic percent of Cd and S on bare CdS and surface sulfur vacancy content of bare CdS and CdS_{S_v}.

Sample	Atomic % of S	Atomic % of Cd	S _v
Bare CdS	49.97	50.03	0.001
CdS S _v	49.25	50.74	0.029

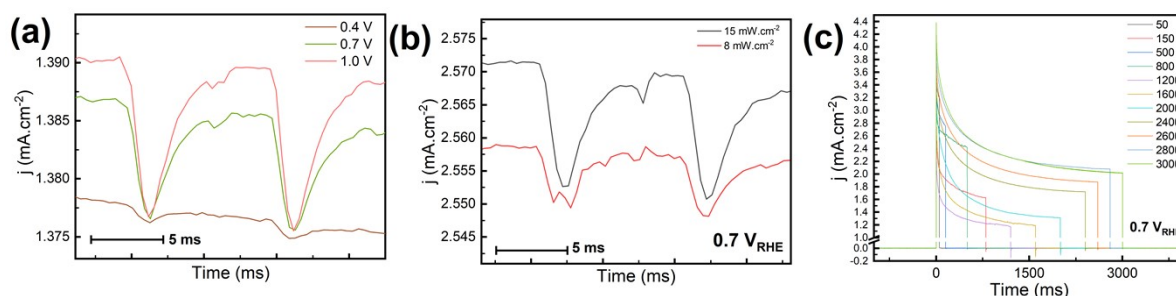


Figure S11. (a) Potential and (b) illumination intensity-dependent periodic cathodic events observed for base CdS under illumination. TPC behavior of CdS at different LED illumination times at 0.7 V.

References

- 1 Z. Song, X. Zhu, Y. Zeng, A. Wang, S. Li, Y. Fan, M. Cai, Q. Cheng, Y. Wei and S. Sun, Cobalt Phosphate Cocatalyst Loaded-CdS Nanorod Photoanode with Well-Defined Junctions for Highly Efficient Photoelectrochemical Water Splitting, *Catal Lett*, 2020, **150**, 1878–1889.
- 2 E. Alkuam, M. Mohammed and T.-P. Chen, Fabrication of CdS nanorods and nanoparticles with PANI for (DSSCs) dye-sensitized solar cells, *Solar Energy*, 2017, **150**, 317–324.
- 3 Y.-J. Dong, J.-F. Liao, Z.-C. Kong, Y.-F. Xu, Z.-J. Chen, H.-Y. Chen, D.-B. Kuang, D. Fenske and C.-Y. Su, Conformal coating of ultrathin metal-organic framework on semiconductor electrode for boosted photoelectrochemical water oxidation, *Applied Catalysis B: Environmental*, 2018, **237**, 9–17.
- 4 Q. Zhao, Z. Liu, Z. Guo, M. Ruan and W. Yan, The collaborative mechanism of surface S-vacancies and piezoelectric polarization for boosting CdS photoelectrochemical performance, *Chemical Engineering Journal*, 2022, **433**, 133226.
- 5 S. Niu, S. Li, Y. Du, X. Han and P. Xu, How to Reliably Report the Overpotential of an Electrocatalyst, *ACS Energy Lett.*, 2020, **5**, 1083–1087.
- 6 H. S. Mahdi, A. Parveen, S. Agrawal and A. Azam, Microstructural and optical properties of sol gel synthesized CdS nano particles using CTAB as a surfactant, *AIP Conference Proceedings*, 2017, **1832**, 050012.
- 7 S. Hong, E. Kim, D.-W. Kim, T.-H. Sung and K. No, On measurement of optical band gap of chromium oxide films containing both amorphous and crystalline phases, *Journal of Non-Crystalline Solids*, 1997, **221**, 245–254.
- 8 P. Makuła, M. Pacia and W. Macyk, How To Correctly Determine the Band Gap Energy of Modified Semiconductor Photocatalysts Based on UV–Vis Spectra, *J. Phys. Chem. Lett.*, 2018, **9**, 6814–6817.
- 9 D. Devadiga, M. Selvakumar, P. Shetty and M. S. Santosh, The integration of flexible dye-sensitized solar cells and storage devices towards wearable self-charging power systems: A review, *Renewable and Sustainable Energy Reviews*, 2022, **159**, 112252.
- 10 H. She, P. Yue, J. Huang, L. Wang and Q. Wang, One-step hydrothermal deposition of F:FeOOH onto BiVO₄ photoanode for enhanced water oxidation, *Chemical Engineering Journal*, 2020, **392**, 123703.
- 11 M. T. Ehrensberger and J. L. Gilbert, A time-based potential step analysis of electrochemical impedance incorporating a constant phase element: A study of commercially pure titanium in phosphate buffered saline, *Journal of Biomedical Materials Research Part A*, 2010, **93A**, 576–584.
- 12 Y. Y. Proskuryakov, K. Durose, M. K. Al Turkestani, I. Mora-Seró, G. Garcia-Belmonte, F. Fabregat-Santiago, J. Bisquert, V. Barrioz, D. Lamb, S. J. C. Irvine and E. W. Jones, Impedance spectroscopy of thin-film CdTe/CdS solar cells under varied illumination, *Journal of Applied Physics*, 2009, **106**, 044507.